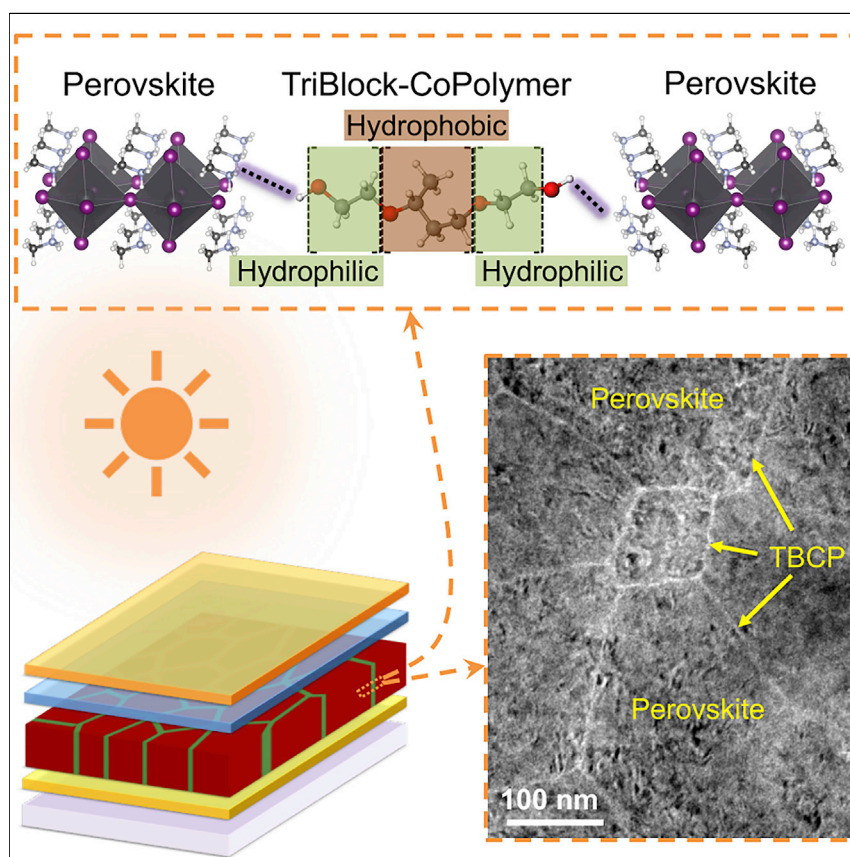


Article

Continuous Grain-Boundary Functionalization for High-Efficiency Perovskite Solar Cells with Exceptional Stability



Grain boundaries in polycrystalline thin films of hybrid perovskites can play a key role in determining the performance and stability of perovskite solar cells. Here, we demonstrate the controlled, continuous grain-boundary functionalization of hybrid perovskite thin films with a rationally selected triblock copolymer with dual hydrophobic-hydrophilic functionalities. This unique grain-boundary structure is responsible for the enhanced optoelectronic properties and environmental stability of these thin films. We also show that the resulting perovskite solar cells are highly efficient and stable.

Yingxia Zong, Yuanyuan Zhou, Yi Zhang, ..., Shuping Pang, Xiao Cheng Zeng, Nitin P. Padture

yuanyuan_zhou@brown.edu (Y.Z.)
pangsp@qibebt.ac.cn (S.P.)
nitin_padture@brown.edu (N.P.P.)

HIGHLIGHTS

Continuous grain-boundary functionalization in hybrid perovskite films is achieved

Dual-function hydrophilic-hydrophobic triblock copolymer is the functionalizing agent

Film optoelectronic properties and environmental stability are enhanced simultaneously

The resulting perovskite solar cells are highly efficient and stable



Article

Continuous Grain-Boundary Functionalization for High-Efficiency Perovskite Solar Cells with Exceptional Stability

Yingxia Zong,^{1,4} Yuanyuan Zhou,^{1,4,*} Yi Zhang,¹ Zhipeng Li,² Lin Zhang,¹ Ming-Gang Ju,³ Min Chen,¹ Shuping Pang,^{2,*} Xiao Cheng Zeng,³ and Nitin P. Padture^{1,5,*}

SUMMARY

Here, we successfully demonstrate the continuous functionalization of grain boundaries (GBs) in $\text{CH}_3\text{NH}_3\text{PbI}_3$ (MAPbI₃) organic-inorganic halide perovskite (OIHP) thin films with a triblock copolymer that contains rationally selected hydrophilic-hydrophobic-hydrophilic symmetric blocks. The addition of the triblock copolymer into the precursor solution assists in perovskite solution crystallization, resulting in ultrasmooth thin films with GB regions that are continuously functionalized. Tuning of the thickness of the functionalized GBs is realized, leading to MAPbI₃ OIHP thin films with simultaneously enhanced optoelectronic properties and environmental (thermal, moisture, and light) stability. The resulting perovskite solar cells show high stabilized efficiency of 19.4%, most of which is retained (92%) upon 480-hr 1-sun illumination. This approach is generic in nature, and it can be extended to a wide range of OIHPs and beyond.

INTRODUCTION

Organic-inorganic halide perovskites (OIHPs) are a family of materials that are revolutionizing the field of photovoltaics (PVs).^{1–4} The record power conversion efficiency (PCE) of perovskite-based solar cells (PSCs) is now ~23% since their invention in 2009.^{1,4} Methylammonium lead triiodide ($\text{CH}_3\text{NH}_3\text{PbI}_3$ or MAPbI₃) is the most typical OIHP used in PSCs.^{1,2,4,5} In the past few years, significant effort has been devoted to controlling the solution crystallization of phase-pure MAPbI₃ thin films for higher-PCE PSCs.^{5,6} Although the research in this direction has been proven to be highly successful, the stability of phase-pure MAPbI₃ under moisture, thermal, and light stresses has become a pressing issue because it determines the overall device stability, which affects the potential commercial deployment of PSCs.^{7–9} Strategies such as encapsulating the whole PSC and engineering MAPbI₃ top and bottom surfaces or interfaces are most commonly used to improve the device stability.^{10–15} These extrinsic strategies prevent the MAPbI₃ film surfaces from interacting with the atmosphere, and have shown promise. However, they do not provide intrinsic solutions for retarding the degradation of MAPbI₃ throughout the thin film.

Grain boundaries (GBs) are the most prominent microstructural feature in solution-processed MAPbI₃ OIHP thin films, which are typically polycrystalline.^{5,6} Wrong or dangling bonds proliferate the GB regions, and they can become easy highways for rapid diffusion of atomic, ionic, and molecular species.^{16,17} GBs can also trap moisture and gas or solvent molecules during the solution processing of MAPbI₃

The Bigger Picture

Organic-inorganic halide perovskites (OIHPs) are a family of crystalline semiconducting materials that are revolutionizing the field of photovoltaics. The grain boundary (GB) is the most prominent microstructural feature in solution-processed polycrystalline OIHP thin films, and GB chemistry plays a key role in achieving efficient stable perovskite solar cells (PSCs). In this study, we demonstrate the continuous chemical functionalization of GBs in OIHP thin films by using a triblock copolymer that exhibits both hydrophilicity and hydrophobicity. This chemical approach significantly boosts the optoelectronic properties and stability of the OIHP thin films, leading to PSCs with 19.4% efficiency and exceptional stability. The concept of continuous GB functionalization is generic, and it is applicable to a broad range of OIHPs and other polycrystalline materials, representing a new direction in the development of high-performance PSCs and other optoelectronic devices.

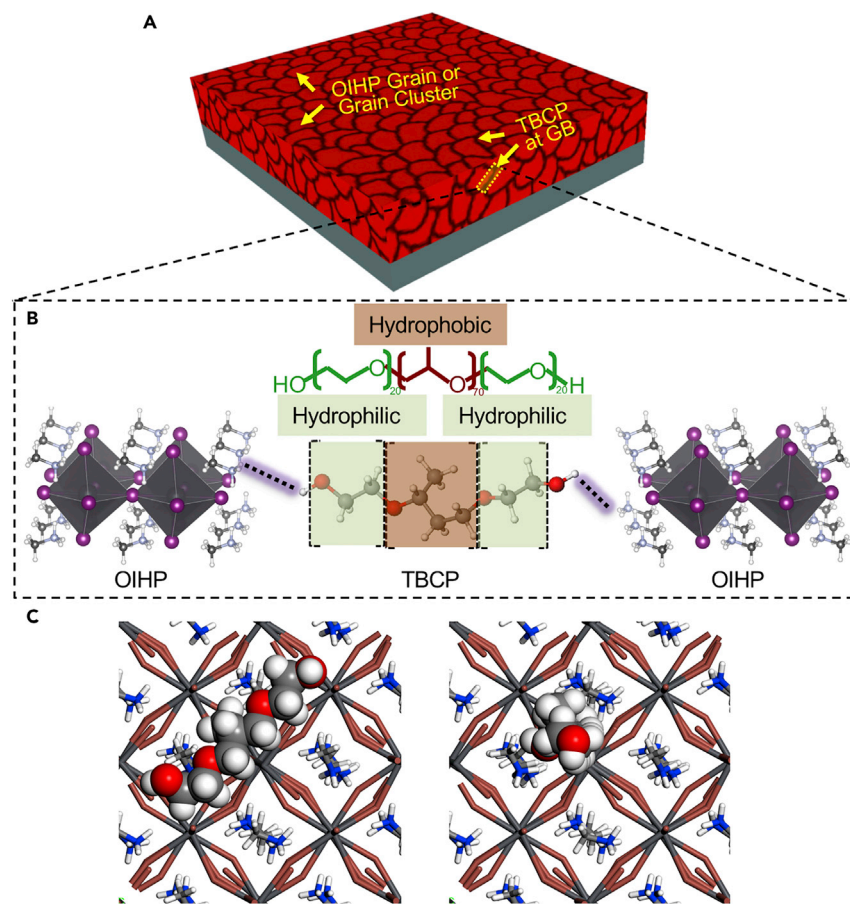


Figure 1. Schematic Illustrations and Structural Models

(A) Schematic illustration of the thin-film structure of MAPbI₃ OIHP with nanoscale TBCP phase continuously functionalizing the GBs, forming GB “walls.”

(B) Schematic illustration of molecular interaction of TBCP with the MAPbI₃ OIHP.

(C) Structural models used for calculating the interaction energy: simplified P123 molecule with the chain direction in plane of (left) or normal to (right) the MAPbI₃ crystal surface.

thin films. Thus, GBs are the most susceptible to thermal, moisture, and light stresses, and it is natural that the propagation of MAPbI₃ degradation occurs favorably along the weakest GB regions in thin films. Therefore, it is of paramount importance to protect the GBs at the nanoscale and create robust OIHP thin-film structures that are intrinsically resistant to moisture, thermal, and light stresses. In this context, a few studies have involved the formation of composites of MAPbI₃ with polymers such as poly(ethylene glycol) and polyvinylpyrrolidone to enhance MAPbI₃ stability, where a polymer scaffold is formed to protect MAPbI₃ from degradation.^{18–20} However, these randomly incorporated insulating polymers can retard carrier transport and also reduce optical absorption of the films. Very recently, Zuo et al.¹⁸ demonstrated high-performance PSCs by using polymer-modified OIHP thin films, but there is still a lack of direct evidence for continuous GB functionalization. Here, we demonstrate, with direct evidence, the successful preparation of a rationally engineered thin-film structure in MAPbI₃ OIHP, where the GBs are continuously functionalized with a polymer phase to form nanoscale GB walls (Figure 1A). Optimizing the GB wall thickness results in the passivation of GBs, which not only significantly improves the tolerance of the MAPbI₃ thin films to environmental (moisture, thermal,

¹School of Engineering, Brown University, Providence, RI 02912, USA

²Qingdao Institute of Bioenergy and Bioprocess Technology, Chinese Academy of Sciences, Qingdao 266101, China

³Department of Chemistry, University of Nebraska - Lincoln, Lincoln, NE 68588, USA

⁴These authors contributed equally

⁵Lead Contact

*Correspondence: yuanyuan_zhou@brown.edu (Y.Z.), pangsp@qibebt.ac.cn (S.P.), nitin_padtare@brown.edu (N.P.P.)

<https://doi.org/10.1016/j.chempr.2018.03.005>

and light) stresses but also enhances their optoelectronic properties. Consequently, PSCs based on this MAPbI₃ OIHP thin-film structure show a high stabilized PCE of 19.4% and exceptional environmental stability.

RESULTS AND DISCUSSION

Three important design criteria for the rational selection of the polymer phase are used in order to form the desired OIHP thin-film microstructure shown in Figure 1A. First, the polymer should exhibit hydrophilicity, which allows its full dissolution and dispersion in the OIHP precursor solutions (in polar solvents). During subsequent solution crystallization, the polymer interacts with the OIHP precursors, and then the OIHP solids, finally forming homogeneous structures through strong molecular interactions (e.g., hydrogen bonding). Second, the polymer should also exhibit hydrophobicity, which is key to resisting ingress of moisture into the OIHP thin films along the GBs. Third and finally, the thickness of the insulating intergranular polymer at the GB needs to be controlled in order to have a benign overall effect on the optoelectronic properties of the OIHP thin films. Using these criteria, we have identified a triblock copolymer (TBCP), where the desirable hydrophilicity and hydrophobicity can be tailored, as the ideal candidate.²¹ TBCPs also have a lower molecular weight than other polymers, allowing functionalization of the OIHP GBs with TBCP of controllable nanoscale thicknesses.

TBCPs are readily available commercially, and the most typical TBCP is Pluronic P123 (PEG-PPG-PEG). P123 comprises poly(ethylene oxide) (PEO) tails and a poly(propylene oxide) (PPO) core. The PPO block exhibits hydrophobicity at temperatures above 288 K, whereas PEO tails are hydrophilic. As shown schematically in Figure 1B, the hydrophilic PEO tails are expected to interact with the polar MA⁺ cation in the MAPbI₃ grains, which enables the assembly of highly uniform P123 phases, functionalizing all the MAPbI₃ GBs throughout the thin film and forming a P123/MAPbI₃ heterostructure interface at each GB. Given the symmetric molecular structure with two PEO tails, P123 is most likely to function as bridges between MAPbI₃ grains when only monolayers of P123 molecules are formed. Meanwhile, the hydrophobic PPO core between the two MAPbI₃ grains is expected to form a moisture-repelling GB network in the thin films. The interaction energies of P123 with MAPbI₃ have been calculated by density functional theory (DFT). A simplified P123 molecule was used because of the expense of the calculations. In determining the most energetically favorable P123/MAPbI₃ heterostructure, two model configurations were considered (Figure 1C). In the first configuration, the simplified P123 molecule chain lies in the plane of the MAPbI₃ crystal surface. The second configuration has the molecule chain normal to the MAPbI₃ crystal surface with the PEO tail pointing into the grain. The hydrogen-bond strengths were computed to be 42 meV and 65 meV for the in-plane and the normal configurations, respectively. This indicates that the P123 molecules will tend to interact strongly with the MAPbI₃ crystalline grains with their PEO tails pointing into the grains, which is the desired configuration.

The solubility of P123 in a typical MAPbI₃ precursor solution (40 wt % in dimethylformamide [DMF]) is very high. Up to 10 wt % P123 can be fully dissolved, resulting in a clear solution (Figure S1) that is stable. Figure S2 compares the UV-vis spectra of the MAPbI₃ precursor solution without and with the addition of 0.5 wt % P123. At the same precursor concentration, the intensity of the absorption peak (~322 nm) that is assigned to the [PbI₂L₄] complex increases (L is the ligand that coordinates with Pb), and the intensity of the [PbI₃L₃]⁻ absorption peak (~363 nm) becomes less

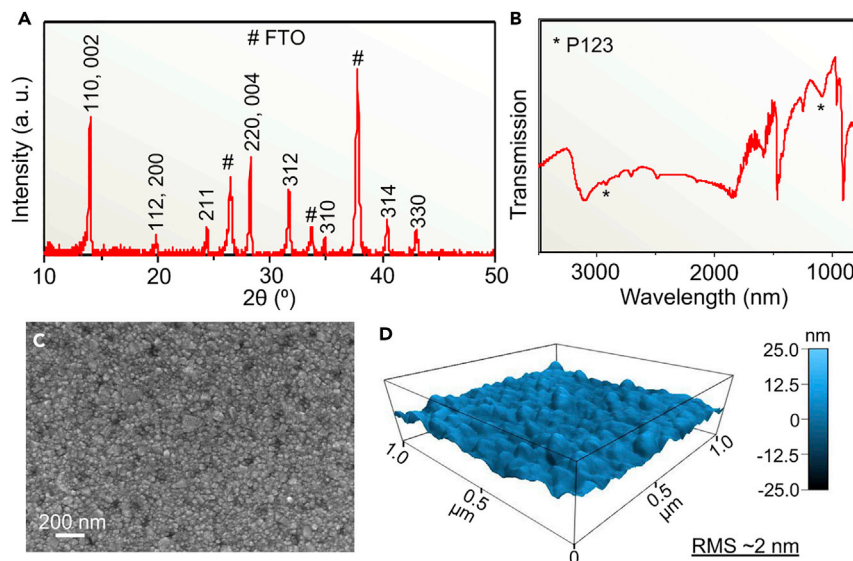


Figure 2. Characterization of P123-Incorporated MAPbI₃-0.5P OIHP Thin Film

Indexed XRD pattern (A), FTIR spectrum (B), SEM image (C, top surface), and AFM image (D, top surface).

resolved. This change in absorption suggests that the added P123 molecules interact with the ions and thus affect the coordination state of Pb ions in the precursor solution.²² It is also natural that the hydrophilic PEO tails in P123 interact with MA⁺ ions and the polar solvent (DMF) in the solution. These chemical interactions are imperative for obtaining uniform heterostructures at the nanoscale through solution-based assembly processes.²³

The P123-passivated MAPbI₃ thin films were prepared by the one-step solution processing method based on (anti)solvent-solvent extraction.^{24,25} Four typical samples of MAPbI₃-0P, MAPbI₃-0.5P, MAPbI₃-1.0P, and MAPbI₃-10P were prepared, which correspond to MAPbI₃ thin films made from precursor solutions with the addition of 0, 0.5, 1.0, and 10 wt % P123, respectively. Figure 2A shows the indexed X-ray diffraction (XRD) pattern of a representative MAPbI₃-0.5P thin film. All observed XRD reflections are associated with the MAPbI₃ OIHP and are indexed as such. No diffraction peaks were observed for P123 because it is amorphous. Figure S3 shows the featureless XRD pattern of phase-pure P123, confirming its amorphous nature. The Fourier-transform infrared spectrum (FTIR) of the MAPbI₃-0.5P sample is shown in Figure 2B. The characteristic bands at $\sim 1,100$ and $\sim 2,900$ cm⁻¹, which are assigned to C–O–C and C–H stretching vibrations in P123, respectively, were observed (Figure S4),²⁶ which indicates the presence of P123 in this thin film; additional bands associated with MAPbI₃ were also observed (Figure 2B). The top-view scanning electron microscopy (SEM) image of the MAPbI₃-0.5P thin film in Figure 2C shows a highly uniform compact microstructure, which is further confirmed by the cross-sectional SEM image in Figure S5. The corresponding atomic force microscopy (AFM) image in Figure 2D shows that the MAPbI₃-0.5P thin film is ultrasmooth with a root-mean-square (RMS) roughness of only ~ 2 nm, a value smaller than that of the smoothest OIHP thin films reported in the literature so far.^{27,28} Figure S6 presents an AFM image of the P123-free MAPbI₃-0P thin film, which shows a typical RMS roughness of ~ 7 nm. Such uniformity and smoothness of the thin-film structure originate from the beneficial effect of P123 in the solution crystallization behavior of MAPbI₃ OIHP. To understand this effect better, we compare XRD patterns and SEM surface morphologies of the four films (MAPbI₃-0P, MAPbI₃-0.5P, MAPbI₃-1.0P, and

MAPbI₃-10P) in Figures S7 and S8, respectively. Although all XRD patterns show phase-pure MAPbI₃ OIHP, the intensities and full-width-at-half-maxima of the XRD peaks (e.g., 110 reflection) decrease gradually with increasing amounts of P123, as shown in Figure S9. Correspondingly, the grain size in P123-passivated MAPbI₃ thin films is reduced with increasing amounts of P123. This implies that the P123 molecules might act as heterogeneous nucleation sites for the crystallization of MAPbI₃ thin films, which enhances the density of nuclei, resulting in the ultrafine grain structure.⁶ The enhancement in the heterogeneous nucleation of MAPbI₃ by the P123 phase also eliminates the occurrence of occasional pinholes in the thin film over large areas (Figure S10), which is consistent with the report by Biet al.²⁸ This leads to the enhanced absorption in the MAPbI₃-0.5P thin film (Figure S11). We further prepared MAPbI₃-0P, MAPbI₃-0.5P, MAPbI₃-1.0P, and MAPbI₃-10P thin films by using the conventional one-step solution method without the antisolvent treatment. The thin-film coverage increases substantially with more addition of P123 (Figure S12), which further confirms the beneficial role of P123 in enhancing the MAPbI₃-nuclei density.

We used transmission electron microscopy (TEM) to examine the detailed nanoscale structures in P123-functionalized MAPbI₃ OIHP thin films. The TEM specimens were prepared by solution-depositing the thin films directly onto carbon-coated TEM grids. This TEM specimen-preparation method minimizes damage to the relatively soft MAPbI₃ OIHP, which can occur during other specimen-preparation procedures such as focused ion beam, and its efficacy has been confirmed by us^{29,30} and others.³¹ Figure 3A is a lower-magnification bright-field TEM image showing the overall microstructure of the MAPbI₃-0.5P thin film. The crystalline MAPbI₃ grains or grain clusters and the P123-functionalized GB walls can be immediately differentiated by the image contrast labeled in Figure 3A. High-resolution TEM images of the MAPbI₃-0P, MAPbI₃-0.5P, MAPbI₃-1.0P, and MAPbI₃-10P thin films are shown in Figures 3B–3E, respectively. The P123-free MAPbI₃-0P thin film is fully crystalline and has no obvious amorphous regions at GBs. The P123-functionalized thin films clearly show the presence of amorphous walls of P123 between the MAPbI₃ grains. Figure S13 presents a more detailed view of the GB regions in the TEM images, where the crystalline and amorphous phases are very clear. Note that the carbon-coated TEM grids used here have amorphous carbon film with holes, which allows part of the specimen thin films to be free standing (substrate-free) (Figure S14); all TEM images were obtained in such free-standing thin films. Thus, the amorphous region observed in Figures 3B–3E does not belong to the carbon films of the TEM grids. It can also be seen that as more P123 was added, the amorphous GB walls grew thicker. The addition of 0.5 and 1.0 wt % P123 in MAPbI₃-0.5P and MAPbI₃-1.0P thin films, respectively, resulted in an average GB thickness of ~3 and ~5 nm, respectively. However, when the amount of P123 was significantly high (MAPbI₃-10P), nanocrystals of MAPbI₃ were formed. These results are consistent with the XRD and SEM results presented in Figures S7 and S8. Electron-energy loss spectra (EELS) were obtained from amorphous and crystalline regions, respectively. As shown Figure 3F, EELS peaks associated with oxygen were observed only in the P123 GB walls but not in or on the crystalline grains (see more EELS results in Figure S15). This further confirms the presence of P123 in the GB regions of the P123-passivated MAPbI₃ OIHP thin films.

It appears that, as the MAPbI₃ OIHP crystals nucleate and grow, P123 molecules are pushed to the regions between the nuclei because P123 cannot be incorporated within the MAPbI₃ crystals. The strong interaction between the orthogonal P123 PEO tails and the MAPbI₃ crystal surfaces ensures that the P123 will functionalize most MAPbI₃ crystal surfaces uniformly and be immobilized rather than agglomerate

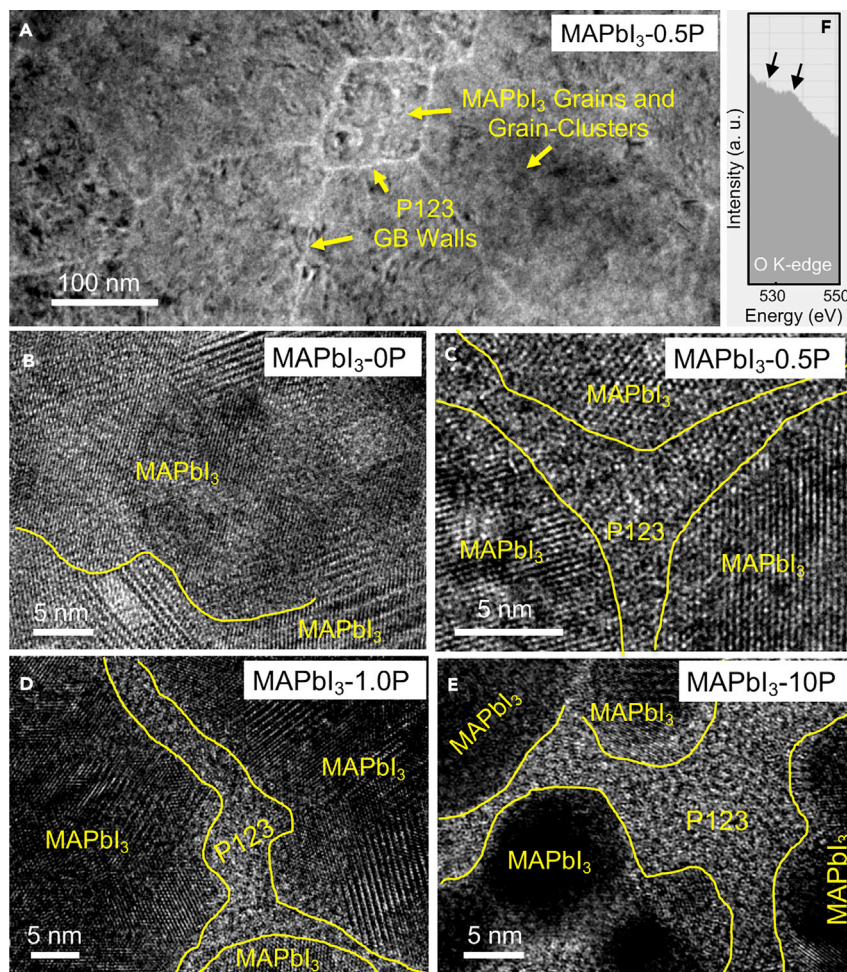


Figure 3. TEM Characterization of P123-Incorporated MAPbI₃ OIHP Thin Films

(A) Low-magnification TEM image of the MAPbI₃-0.5P thin film. (B–E) High-resolution TEM images of thin films: (B) MAPbI₃-0P, (C) MAPbI₃-0.5P, (D) MAPbI₃-1.0P, and (E) MAPbI₃-10P. All thin films were deposited directly on the TEM grids. The yellow lines demarcate GB regions. (F) EELS spectrum (O K-edge, arrows) obtained from the light-contrast P123 region.

into pockets. As the MAPbI₃ grains grow further, the P123 will continue to concentrate into the narrowing intergranular regions between the grains or grain clusters. Eventually, the segregated P123 will form the GB walls between the MAPbI₃ grains or grain clusters. Thus, the hydrophilic nature of the PEO tails and their strong interaction with the MAPbI₃ crystal surfaces, as shown schematically in Figure 1, are key to obtaining the uniform dispersion of P123 GB walls within the MAPbI₃ OIHP thin-film microstructure.

We used the P123-functionalized MAPbI₃ OIHP thin films to fabricate PSCs and evaluated their PV performance. The most typical PSC architecture was used—a Spiro-OMeTAD/Au cathode and a mesostructured-TiO₂/compact-TiO₂/FTO (fluorine-doped tin oxide) anode, where Spiro-OMeTAD and compact-TiO₂ serve as the hole-transporting layer and the electron-transporting layer, respectively. The cross-sectional SEM image of a typical PSC is shown in Figure 4A, where false colors delineate each layer in the PSC. Figure 4B shows typical current density-voltage (*J*-*V*)

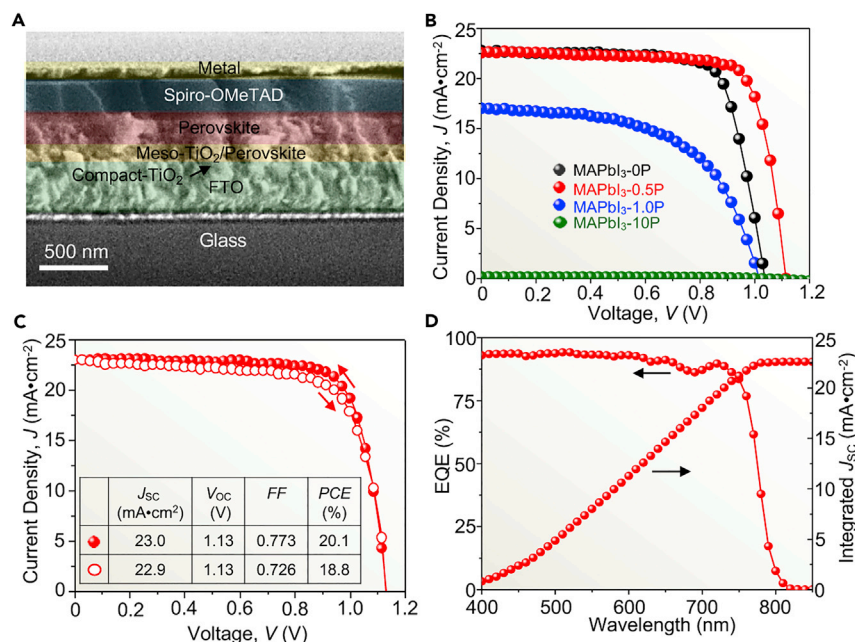


Figure 4. PSCs and Their Photovoltaic Performance

(A) SEM image (false color) showing the cross-section of a typical PSC made with MAPbI₃-0.5P thin film.

(B) Typical J-V curves (reverse scan) of PSCs made with MAPbI₃-0P, MAPbI₃-0.5P, MAPbI₃-1.0P, and MAPbI₃-10P thin films. Extracted PV performance parameters are included in Table S1.

(C) J-V hysteresis of the best-PCE PSC made with MAPbI₃-0.5P thin film. Inset: table of PV performance parameters.

(D) EQE spectrum and integrated J of the best-PCE PSC made with the MAPbI₃-0.5P thin film.

curves (reverse scan) of PSCs made with MAPbI₃-0P, MAPbI₃-0.5P, MAPbI₃-1.0P, and MAPbI₃-10P thin films. The extracted PV performance parameters are included in Table S1. The PSC based on the P123-free MAPbI₃-0P thin film showed a typical good PCE of 17.6% with a short circuit density (J_{SC}) of 22.62 mA cm⁻², open circuit voltage (V_{OC}) of 1.03 V, and fill factor (FF) of 0.755. With the addition of 0.5 wt % P123 in the thin film (MAPbI₃-0.5P), the overall PCE increased to 19.3%, and the V_{OC} was significantly enhanced to 1.11 V. The nanoscale photovoltaic responses of both MAPbI₃-0.5P and MAPbI₃-0P thin films were measured at a typical pinhole-free location with conducting AFM under light, as shown in Figure S16. An enhanced V_{OC} was again observed for MAPbI₃-0.5P, which indicates that V_{OC} enhancement is not only due to the elimination of pinholes in the film (Figure S10) but also attributed to the defect-passivation effect of the GB functionalization with optimal P123 thickness; this is similar to what has been observed in other GB-passivation approaches.^{18,32–34} We then estimated the trap density in MAPbI₃-0.5P by monitoring the evolution of the space-charge-limited current (in dark) as a function of the bias voltage in a capacitor-like device (Figure S17), which showed 30% less than that in MAPbI₃-0P. MAPbI₃-0.5P also exhibited a longer photoluminescence (PL) lifetime than MAPbI₃-0P, as shown in Figure S18, suggesting a reduction of overall non-radiative recombination in the thin film. This is consistent with the less-populated defects and traps in MAPbI₃-0.5P. Further increase in the addition of P123 (MAPbI₃-1.0P and MAPbI₃-10P) had an adverse effect on all the PV performance parameters (Table S1), and no obvious PV response was observed with the addition of 10 wt % P123 (MAPbI₃-10P). This is probably because the very thick P123 GB walls blocked charge transport in the MAPbI₃ thin films. Figure S19 shows the rapid

increase in the film resistivity as a function of the amount of P123. Stabilized maximum-power-point PCE outputs are also included in Figure S20, which shows a consistent trend in the PCE variation with an increase in the P123 amount, although the PCE values are slightly lower than those extracted from the J - V curves. We also made devices by using MAPbI₃ thin films with the incorporation of 0.1 wt % P123; these exhibited a typical PCE of 18.2% (Figure S21), which is lower than that (19.3%) in the case of the incorporation of 0.5 wt % P123. It is highly possible that the GB passivation is less continuous when a very small amount of P123 is used. These results highlight the importance of tailoring the thickness of the functionalized GB regions, and thus P123 is indeed an exceptional candidate for achieving this goal, as shown in Figure 3. The PCE statistics for the MAPbI₃-0.5- and MAPbI₃-0P-based PSCs are compared in Figure S22, which attests to the reproducibility of the P123 effect. The champion PSC made with the MAPbI₃-0.5P thin film showed a PCE of 20.1% (reverse scan) with a high V_{OC} of 1.13 eV and very small hysteretic behavior (18.8% PCE in forward scan). Figure S23 plots the corresponding stabilized maximum-power-point PCE output. A stabilized PCE of 19.4% was reached immediately upon illumination. The external quantum efficiency (EQE) spectrum of the PSC based on MAPbI₃-0.5P thin film gave an integrated J_{SC} value of 22.7 mA cm⁻², which is close to the J_{SC} value extracted from the corresponding J - V curve.

We assessed the environmental stability of the best-performing MAPbI₃-0.5P thin films by subjecting them to three important stress conditions: (1) heat, (2) moisture, and (3) light. The P123-free MAPbI₃-0P thin films were used as a reference. We conducted thermal-stability testing in a N₂-filled glovebox by annealing the thin films on a hotplate at 100°C for 2.5 hr. Moisture-stability testing was performed in a climate chamber (25°C, 70% relative humidity [RH]) for 16 hr. Finally, we conducted light-stability testing by placing the thin films under stimulated AM1.5G 1-sun illumination for 10 hr. For the light-stability tests, we sealed the thin films in a solution-processed poly(methyl methacrylate) (PMMA) coating to minimize the effect of the environment during the testing. All the films were fabricated on TiO₂-coated FTO-glass substrates that are typically used in PSCs. Figures 5A–5C show that, under the same testing conditions, the MAPbI₃-0.5P thin film retained the high purity of the MAPbI₃ OIHP phase, whereas significant MAPbI₃-to-PbI₂ decomposition was observed in the reference MAPbI₃-0P thin film. This significantly enhanced stability of the MAPbI₃-0.5P thin films over their P123-free counterpart is directly attributed to the presence of the intergranular P123 GB walls and demonstrates the simultaneous electronic and environmental passivation effects. In order to understand this environmental stability effect, we recorded a sequence of SEM images during the progression of the degradation of the MAPbI₃-0P and MAPbI₃-0.5P thin films upon annealing in the ambient (Figure S24). In the P123-free MAPbI₃-0P reference thin film, platelet-like PbI₂ crystals appeared to evolve mainly at the GB regions, and they became populated rapidly with time. In the case of MAPbI₃-0.5P thin film, only a few PbI₂ platelets were visible after 7 hr. Also, there was no clear correlation between the location of the PbI₂ platelets and the original film microstructure. Under such severe environmental conditions, even after 52 hr, the MAPbI₃-0.5P thin film still contained a certain amount of undamaged MAPbI₃ grains, whereas the MAPbI₃-0P thin film had completely transformed to PbI₂ (Figure S25). These observations further confirm the beneficial effect of continuous GB functionalization on the environmental stability of MAPbI₃ OIHP thin films.

Figure 5D compares the operational stability of PSCs based on MAPbI₃-0P and MAPbI₃-0.5P thin films. Both PSCs (unencapsulated) were tested under a controlled dry atmosphere (Experimental Procedures) for a total of 480 hr. J - V scans were performed every 2 hr. For the P123-free MAPbI₃-0P thin film, the PCE decreased

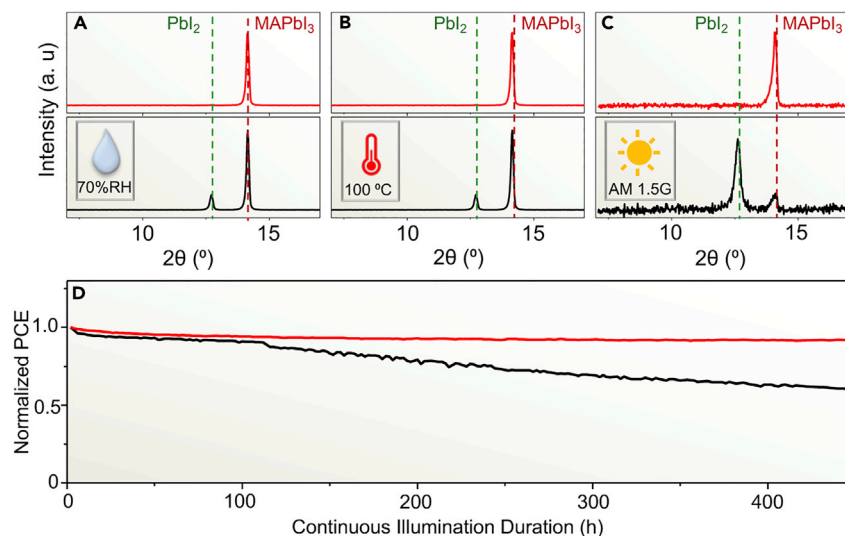


Figure 5. Stability of P123-Incorporated MAPbI₃ OIHP Thin Films and PSCs

(A–C) XRD patterns comparing the stability of MAPbI₃-0P (black) and MAPbI₃-0.5P (red) thin films after being subjected to environmental stress: (A) moisture (70% RH at 25°C for 16 hr), (B) thermal (dry N₂ atmosphere at 100°C for 2.5 hr), and (C) light (AM1.5G 1-sun for 10 hr while encapsulated in PMMA).

(D) Comparison of the operational stability of PSCs (unencapsulated) made with MAPbI₃-0P (black) and MAPbI₃-0.5P (red) thin films under continuous AM1.5G 1-sun illumination.

continuously with prolonged illumination such that 59% of the original PCE was retained after 480 hr. In contrast, the PSC made with MAPbI₃-0.5P thin film showed stable PCE and retained 92% of the original PCE after 480 hr under illumination. We further compared the stability of PSCs based on MAPbI₃-0P and MAPbI₃-0.5P thin films after 30-day storage in ambient air (25% RH, room temperature). The results are presented in Figure S26, and they show that the PSCs based on MAPbI₃-0.5P thin films had significantly higher PCE retention (92%) than those based on MAPbI₃-0P (80%). This provides direct evidence of the beneficial effect of P123 incorporation on PSC stability.

Conclusion

We have successfully realized controlled, continuous GB functionalization of MAPbI₃ perovskite thin films through the rational incorporation of the P123 triblock copolymer phase with hydrophilic-hydrophobic-hydrophilic symmetric blocks. The continuous GB functionalization not only leads to enhanced optoelectronic properties in the ultrasoft thin films but also imparts significant resistance against moisture, heat, and light stresses. Consequently, the resulting PSCs have both high PCE and exceptional stability. We envision that the general concept of GB functionalization presented here will complement the widely studied composition engineering strategies for halide perovskites,^{35–38} leading to future PSCs with superior PCE and environmental stability suitable for the market.

EXPERIMENTAL PROCEDURES

Materials Synthesis and Film Fabrication

MAPbI₃-0P, MAPbI₃-0.5P, MAPbI₃-1P, and MAPbI₃-10P OIHP thin films were prepared by the (anti)solvent-assisted one-step spin-coating method.²⁴ A base MAPbI₃-0P precursor solution of 40 wt % concentration was prepared by co-dissolving 0.461 g of PbI₂ (99.9985%, Alfa Aesar, USA) and 0.159 g of MAI (Dyesol, Australia) in 0.930 g of DMF (Sigma-Aldrich, USA) solvent. For the preparation of

MAPbI₃-0.5P, MAPbI₃-1P, and MAPbI₃-10P solutions, 0.003, 0.006, and 0.031 g of Pluronic P123 was added, respectively. Subsequently, the precursor solutions were spin-coated at 4,000 rpm for 30 s on appropriate substrates. At 7 s after the start of the spin-coating step, 0.6 mL of chlorobenzene was quickly dripped. The spin-coated thin films were then annealed at 130°C for 5 min.

Material and Film Characterization

XRD patterns were obtained under Cu K_α radiation ($\lambda = 0.15406$ nm) with a step size of 0.02° on an X-ray diffractometer (Bruker D8-advance, Karlsruhe, Germany). The surface morphology of the thin films was characterized by SEM (LEO 1530VP, Carl Zeiss, Germany). The local roughness of the thin films was characterized by AFM (MFP-3D Origin, Asylum Research, USA) with a silicon probe. Conductive AFM measurements were made with the same instrument in contact mode with a conducting platinum-coated silicon probe (Econo-SCM-PIC, Asylum Research, USA). UV-vis spectra were obtained with a spectrophotometer (UV-2600, Shimadzu, Japan) equipped with an integrating sphere attachment (ISR-2600, Shimadzu, Japan). A standard BaSO₄ pellet (Nacalai Tesque, Japan) was used as the reference. UV-vis spectra of the solutions were obtained with the same spectrophotometer without the integrating sphere attachment. FTIR spectra were obtained on a spectrometer (4100, Jasco Instruments, USA). Samples for the FTIR measurements were prepared by scratching the thin films from the substrates.

DFT Computation

Atomistic simulations at the DFT level were performed with CP2K 3.0 code and the hybrid Gaussian and plane-wave method implemented in the Quickstep module. The Perdew-Burke-Ernzerhof functional with Grimme correction was adopted to describe the dispersion interactions. A mixed Gaussian basis set (DZVP-MOLOPT) and norm-conserving GTH pseudopotentials were used on all atoms. The binding energy (E_{Binding}) is defined by $E_{\text{Binding}} = E_{\text{Perovskite}} + E_{\text{P123}} - E_{\text{Perovskite-P123}}$, where $E_{\text{Perovskite}}$, E_{P123} , and $E_{\text{Perovskite-P123}}$ are the energies of MAPbI₃, P123, and the whole system (shown in Figure 1C), respectively.

PSC Fabrication and Characterization

FTO-coated glass substrates were patterned by etching with Zn powder and 1 M HCl diluted in distilled water. The etched substrates were first soaked in a saturated KOH ethanol solution for 12 hr and cleaned sequentially with deionized water and ethanol. The substrates were then blow-dried with N₂ gas and were further subjected to UV light. Compact TiO₂ films on the FTO substrates were obtained by spray pyrolysis at 450°C. After cooling down to room temperature, the substrates were then transferred into a N₂-filled glovebox for deposition of the MAPbI₃-OP, MAPbI₃-0.5P, MAPbI₃-1P, or MAPbI₃-10P OIHP thin films according to the above procedure. A hole-transporting material solution was spin-coated on the OIHP films at 4,000 rpm for 30 s; this was prepared by dissolving 80 mg of 2,2',7,7'-tetrakis(*N,N*-di-methoxyphenylamine)-9,9'-spirobifluorene (Spiro-OMETAD, Merck, Germany), 28.8 mL of 4-*tert*-butylpyridine, and 17.5 mL of lithium bis(trifluoromethylsulfonyl) imide (Li-TFSI) solution (520 mg Li-TFSI in 1 mL acetonitrile) in 1 mL of chlorobenzene. Finally, Au electrode was deposited by thermal evaporation to complete the device. The champion PSC was made by optimization of the above fabrication procedures and details with the MAPbI₃-0.5P thin film. The EQE spectra were obtained in AC mode with a solar cell quantum efficiency measurement system (EQE-200, Oriel Instruments, USA). The *J-V* characteristics of the PSCs were measured with a 2400 Sourcemeter (Keithley, USA) under simulated 1-sun AM 1.5G 100 mW cm⁻² intensity (Oriel Sol3A Class AAA, Newport, USA) in both reverse (from V_{OC} to J_{SC}) and forward (from J_{SC} to V_{OC}) scans. The step voltage was 25 mV with

5 ms of delay time per step. A typical active area of 0.12 cm² was defined with a non-reflective mask for the *J-V* measurements.

Long-Term Stability Testing of PSCs

The PSCs were placed in a sealed holder with a transparent glass cover. A flow of Ar gas was continuously passed through the holder to minimize the water and oxygen content in the atmosphere. *J-V* curves were performed every 2 hr. The temperature of the PSCs was maintained at ~40°C under continuous 1-sun illumination. Between the *J-V* measurements, the PSCs were biased at the maximum-power-point voltage with a potentiostat under illumination.

SUPPLEMENTAL INFORMATION

Supplemental Information includes 26 figures and 1 table and can be found with this article online at <https://doi.org/10.1016/j.chempr.2018.03.005>.

ACKNOWLEDGMENTS

Y. Zong, Y. Zhang, M.C., L.Z., Y. Zhou, and N.P.P. were supported by the Office of Naval Research (no. N00014-17-1-2232) and the National Science Foundation (no. OIA-1538893), and they are grateful for that support. S.P. and Z.L. thank the National Natural Science Foundation of China (no. 51672290) and the Chinese Academy of Sciences Youth Innovation Promotion Association (no. 2015167) for support. M.-G.J. and X.C.Z. thank the National Science Foundation (nos. DMR-1420645 and OIA-1538893) and the University of Nebraska Holland Computing Center for the support. We also thank Mr. J. Kwun for his experimental assistance.

AUTHOR CONTRIBUTIONS

Y. Zhou and N.P.P. conceived the idea, designed the experiments, and managed the project. Y. Zong and Y. Zhou conducted the synthesis and characterization experiments. L.Z. and Y. Zhou conducted the TEM experiments. Y. Zhang, Y. Zong, Z.L., and S.P. fabricated the devices. Y. Zhang performed the PSC stability testing. M.C. conducted the AFM experiments. M.-G.J. and X.C.Z. performed the DFT calculations. Y. Zhou and N.P.P. co-wrote the manuscript with comments and contributions from the other co-authors.

DECLARATION OF INTERESTS

The authors declare no competing financial interests.

Received: November 22, 2017

Revised: February 7, 2018

Accepted: March 9, 2018

Published: April 19, 2018

REFERENCES AND NOTES

1. Kojima, A., Teshima, K., Shirai, Y., and Miyasaka, T. (2009). Organometal halide perovskites as visible-light sensitizers for photovoltaic cells. *J. Am. Chem. Soc.* *131*, 6050–6051.
2. Kim, H.-S., Lee, C.-R., Im, J.-H., Lee, K.-B., Moehl, T., Marchioro, A., Moon, S.-J., Baker, R.H., Yum, J.-H., Moser, J.E., et al. (2012). Lead iodide perovskite sensitized all-solid-state submicron thin film mesoscopic solar cell with efficiency exceeding 9%. *Sci. Rep.* *2*, 591.
3. Yang, W.S., Park, B., Jung, E.H., and Jeon, N.J. (2017). Iodide management in formamidinium-lead-halide-based perovskite layers for efficient solar cells. *Science* *356*, 1376–1379.
4. Stranks, S.D., Eperon, G.E., Grancini, G., Menelaou, C., Alcocer, M.J.P., Leijtens, T., Herz, L., Petrozza, A., and Snaith, H.J. (2013). Electron-hole diffusion lengths exceeding 1 micrometer in an organometal trihalide perovskite absorber. *Science* *342*, 341–344.
5. Zhao, Y., and Zhu, K. (2016). Organic-inorganic hybrid lead halide perovskites for optoelectronic and electronic applications. *Chem. Soc. Rev.* *45*, 655–689.
6. Zhou, Y., Game, O.S., Pang, S., and Padture, N.P. (2015). Microstructures of organometal trihalide perovskites for solar cells: their evolution from solutions and characterization. *J. Phys. Chem. Lett.* *6*, 4827–4839.
7. Mei, A., Li, X., Liu, L., Ku, Z., Liu, T., Rong, Y., Xu, M., Hu, M., Chen, J., Yang, Y., et al. (2014). A

- hole-conductor-free, fully printable mesoscopic perovskite solar cell with high stability. *Science* 345, 295–298.
- Nagabhushana, G.P., Shivaramaiah, R., and Navrotsky, A. (2016). Direct calorimetric verification of thermodynamic instability of lead halide hybrid perovskites. *Proc. Natl. Acad. Sci. USA* 113, 7717–7721.
 - Grätzel, M. (2017). The rise of highly efficient and stable perovskite solar cells. *Acc. Chem. Res.* 50, 487–491.
 - Grancini, G., Roldán-Carmona, C., Zimmermann, I., Mosconi, E., Lee, X., Martineau, D., Narbey, S., Oswald, F., De Angelis, F., Graetzel, M., and Nazeeruddin, M.K. (2017). One-year stable perovskite solar cells by 2D/3D interface engineering. *Nat. Commun.* 8, 15684.
 - Tan, H., Jain, A., Voznyy, O., Lan, X., Arquer, F., Fan, J.Z., Bermudez, R., Yuan, M., Zhang, B., Zhao, Y., et al. (2017). Efficient and stable solution-processed planar perovskite solar cells via contact passivation. *Science* 355, 722–726.
 - Yang, Y., and You, J. (2017). Make perovskite solar cells stable. *Nature* 544, 155–156.
 - Chen, W., Wu, Y., Yue, Y., Liu, J., Zhang, W., Yang, X., Chen, H., Bi, E., Ashrafali, I., Grätzel, M., et al. (2015). Efficient and stable large-area perovskite solar cells with inorganic charge extraction layers. *Science* 350, 944–948.
 - Yang, S., Wang, Y., Liu, P., Cheng, Y.-B., Zhao, H.J., and Yang, H.G. (2016). Functionalization of perovskite thin films with moisture-tolerant molecules. *Nat. Energy* 1, 15016.
 - Bella, F., Griffini, G., Correa-Baena, J., Saracco, G., Grätzel, M., Hagfeldt, A., Turri, S., and Gerbaldi, C. (2016). Improving efficiency and stability of perovskite solar cells with photocurable fluoropolymers. *Science* 354, 203–206.
 - Yin, W.-J., Shi, T., and Yan, Y. (2014). Unique properties of halide perovskites as possible origins of the superior solar cell performance. *Adv. Mater.* 26, 4653–4658.
 - Wang, Q., Chen, B., Liu, Y., Deng, Y., Bai, Y., Dong, Q., and Huang, J. (2017). Scaling behavior of moisture-induced grain degradation in polycrystalline hybrid perovskite thin films. *Energy Environ. Sci.* 10, 516–522.
 - Zuo, L., Guo, H., deQuilettes, D.W., Jariwala, S., Marco, N., Dong, S., DeBlock, R., Ginger, D.S., Dunn, B., Wang, M., et al. (2017). Polymer-modified halide perovskite films for efficient and stable planar heterojunction solar cells. *Sci. Adv.* 3, e1700106.
 - Zhao, Y., Wei, J., Li, H., Yan, Y., Zhou, W., Yu, D., and Zhao, Q. (2016). A polymer scaffold for self-healing perovskite solar cells. *Nat. Commun.* 7, 10228.
 - Guo, Y., Shoyama, K., Sato, W., and Nakamura, E. (2016). Polymer stabilization of lead(II) perovskite cubic nanocrystals for semitransparent solar cells. *Adv. Energy Mater.* 6, 1502317.
 - Mai, Y., and Eisenberg, A. (2012). Self-assembly of block copolymers. *Chem. Soc. Rev.* 41, 5969–5985.
 - Stamplecoskie, K.G., Manser, J.S., and Kamat, P.V. (2015). Dual nature of the excited state in organic-inorganic lead halide perovskites. *Energy Environ. Sci.* 8, 208–215.
 - Whitesides, G.M., and Grzybowski, B. (2002). Self-assembly at all scales. *Science* 295, 2418–2421.
 - Jeon, N.J., Noh, J.H., Kim, Y.C., Yang, W.S., Ryu, S., and Seok, S.I. (2014). Solvent engineering for high-performance inorganic-organic hybrid perovskite solar cells. *Nat. Mater.* 13, 897–903.
 - Zhou, Y., Yang, M., Wu, W., Vasiliev, A.L., Zhu, K., and Pature, N.P. (2015). Room-temperature crystallization of hybrid-perovskite thin films via solvent-solvent extraction for high-performance solar cells. *J. Mater. Chem. A* 3, 8178–8184.
 - Wei, X., Su, J., Li, X.-H., and Chen, J.-S. (2014). Chemical “top-down” synthesis of amphiphilic superparamagnetic Fe₃O₄ nanobelts from exfoliated FeOCl layers. *Dalton Trans.* 43, 16173–16177.
 - Raga, S.R., Ono, L.K., and Qi, Y. (2016). Rapid perovskite formation by CH₃NH₂ gas-induced intercalation and reaction of Pbl₂. *J. Mater. Chem. A* 4, 2494–2500.
 - Bi, D., Yi, C., Luo, J., Décoppet, J.-D., Zhang, F., Zakeeruddin, S.M., Li, X., Hagfeldt, A., and Grätzel, M. (2016). Polymer-templated nucleation and crystal growth of perovskite films for solar cells with efficiency greater than 21%. *Nat. Energy* 1, 16142.
 - Zhou, Y., Vasiliev, A.L., Wu, W., Yang, M., Pang, S., Zhu, K., and Pature, N.P. (2015). Crystal morphologies of organolead trihalide in mesoscopic/planar perovskite solar cells. *J. Phys. Chem. Lett.* 6, 2292–2297.
 - Ji, F., Pang, S., Zhang, L., Zong, Y., Cui, G., Pature, N.P., and Zhou, Y. (2017). Simultaneous evolution of uniaxially-oriented grains and ultralow-density grain-boundary network in CH₃NH₃Pbl₃ perovskite thin films mediated by precursor-phase metastability. *ACS Energy Lett.* 2, 1734–1739.
 - Rothmann, M.U., Li, W., Zhu, Y., Bach, U., Spiccia, L., Etheridge, J., and Cheng, Y.-B. (2017). Direct observation of intrinsic twin domains in tetragonal CH₃NH₃Pbl₃. *Nat. Commun.* 8, 14547.
 - Zeng, X., Chen, B., Dai, J., Fang, Y., Bai, Y., Lin, Y., Wei, H., Zeng, X.C., and Huang, J. (2017). Defect passivation in hybrid perovskite solar cells using quaternary ammonium halide anions and cations. *Nat. Energy* 2, 17102.
 - Lee, J.-W., Bae, S.-H., Hsieh, Y.-T., De Marco, N., Wang, M., Sun, P., and Yang, Y. (2017). A bifunctional Lewis base additive for microscopic homogeneity in perovskite solar cells. *Chem* 3, 290–302.
 - Son, D.-Y., Lee, J.-W., Choi, Y.J., Jang, I.-H., Lee, S., Yoo, P.J., Shin, H., Ahn, N., Choi, M., Kim, D., and Park, N.-G. (2016). Self-formed grain boundary healing layer for highly efficient CH₃NH₃Pbl₃ perovskite solar cells. *Nat. Energy* 1, 16081.
 - Wang, Z., Lin, Q., Chmiel, F.P., Sakai, N., Herz, L.M., and Snaith, H.J. (2017). Efficient ambient-air-stable solar cells with 2D-3D heterostructured butylammonium-cesium-formamidinium lead halide perovskites. *Nat. Energy* 2, 17135.
 - Saliba, M., Matsui, T., Domanski, K., Seo, J.-Y., Ummadisingu, A., Zakeeruddin, S.M., Correa-Baena, J., Tress, W.R., Abate, A., Hagfeldt, A., et al. (2016). Incorporation of rubidium cations into perovskite solar cells improves photovoltaic performance. *Science* 354, 206–209.
 - Zhou, Y., Zhou, Z., Chen, M., Zong, Y., Pang, S., and Pature, N.P. (2016). Doping and alloying for improved perovskite solar cells. *J. Mater. Chem. A* 4, 17623–17635.
 - Tsai, H., Nie, W., Blancon, J.-C., Stoumpos, C.C., Asadpour, R., Harutyunyan, B., Neukirch, A.J., Verduzco, R., Crochet, J.J., Tretiak, S., et al. (2016). High-efficiency two-dimensional Ruddlesden-Popper perovskite solar cells. *Nature* 536, 312–316.

Chem, Volume 4

Supplemental Information

Continuous Grain-Boundary Functionalization

for High-Efficiency Perovskite Solar

Cells with Exceptional Stability

Yingxia Zong, Yuanyuan Zhou, Yi Zhang, Zhipeng Li, Lin Zhang, Ming-Gang Ju, Min Chen, Shuping Pang, Xiao Cheng Zeng, and Nitin P. Padture

Supplemental Information

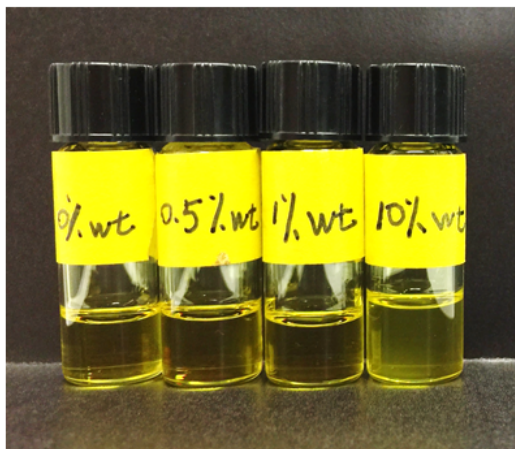


Figure S1. Photographs of MAPbI₃ DMF solutions (40 wt%) containing 0, 0.5, 1.0, and 10 wt% P123.

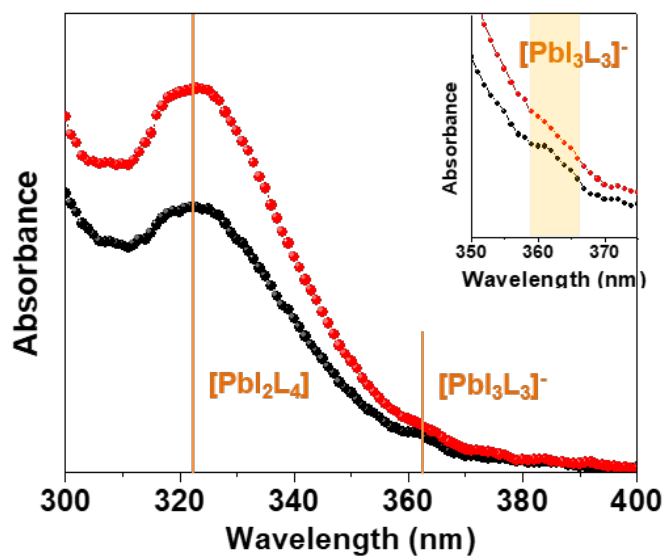


Figure S2. UV-*vis* spectra of MAPbI₃ DMF solutions containing 0 and 0.5 wt% P123. Diluted solutions, with Pb²⁺ concentration of 1.84 nM, were used for the measurements. It is observed that after P123 addition, the absorption peak (~322 nm) that is assigned to [PbI₂L₄] is increased, whereas the absorption (shoulder) peak (~363 nm) becomes less resolved.

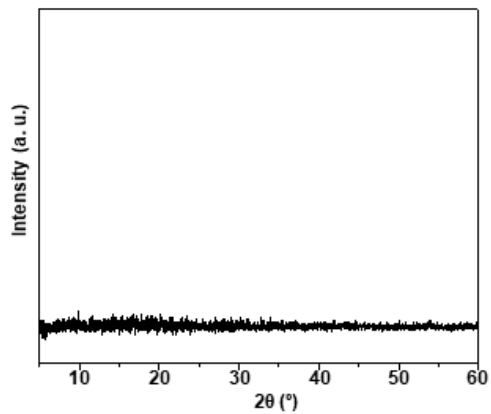


Figure S3. XRD pattern of phase-pure P123.

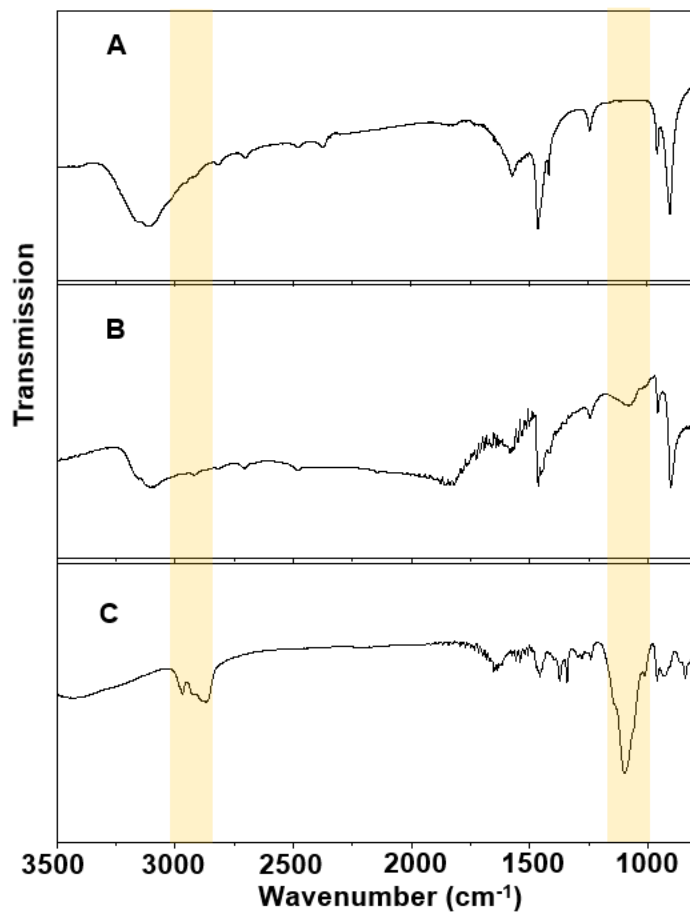


Figure S4. FTIR spectra of (A) phase-pure MAPbI₃, (B) MAPbI₃-0.5P and (C) phase-pure P123 samples. The characteristic bands (alkyl C-H stretching at ~2900 cm⁻¹ and C-OH stretching at ~1100 cm⁻¹) of P123 are highlighted.

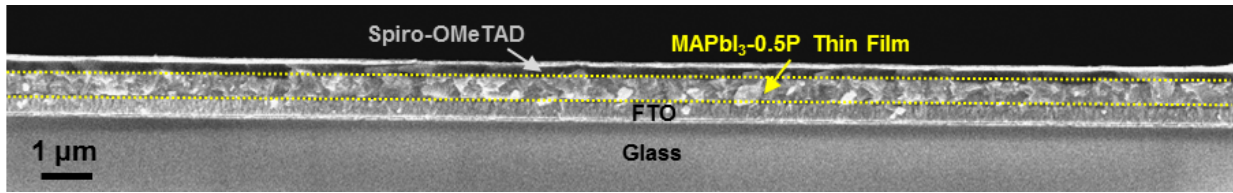


Figure S5. Cross-sectional SEM image of the MAPbI₃-0.5P thin film. The thin film is covered by a thin layer of Spiro-OMeTAD HTL for ease of SEM observation.

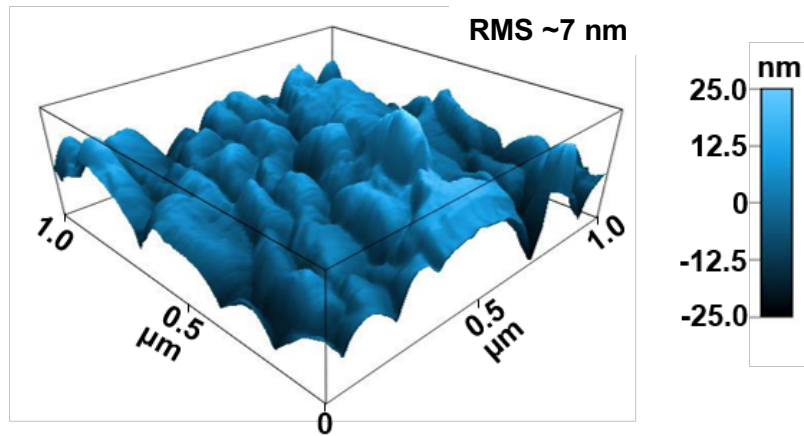


Figure S6. AFM image of the MAPbI₃-0P thin film.

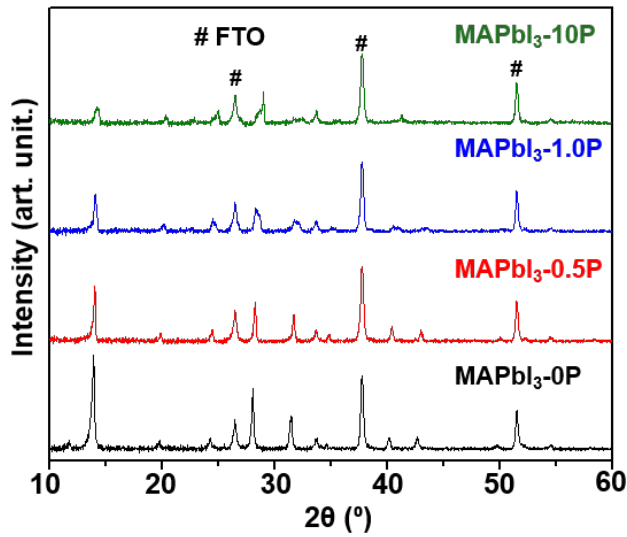


Figure S7. XRD patterns of the MAPbI₃-0P, MAPbI₃-0.5P, MAPbI₃-1.0P, and MAPbI₃-10P thin films.

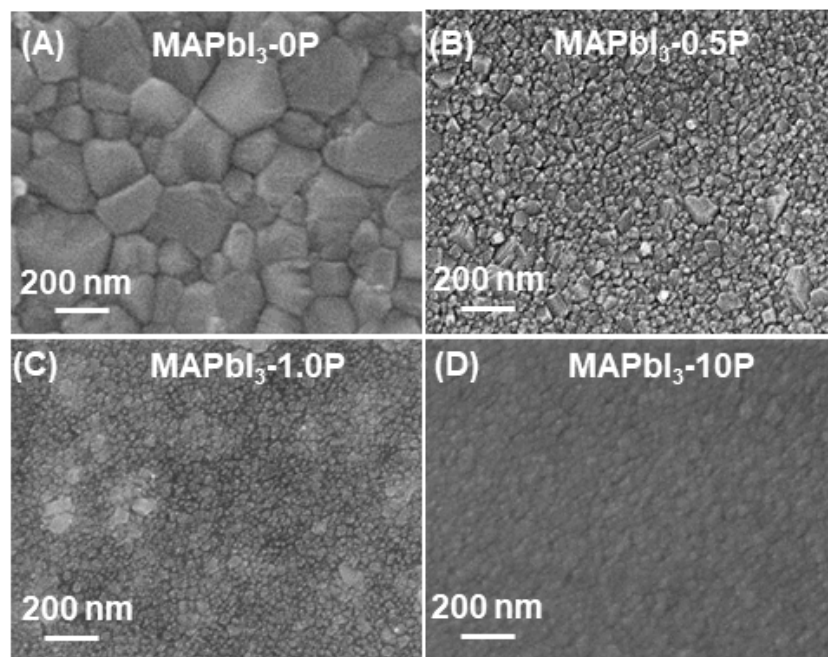


Figure S8. SEM images showing the surface morphologies of the MAPbI₃-0P, MAPbI₃-0.5P, MAPbI₃-1.0P, and MAPbI₃-10P thin films.

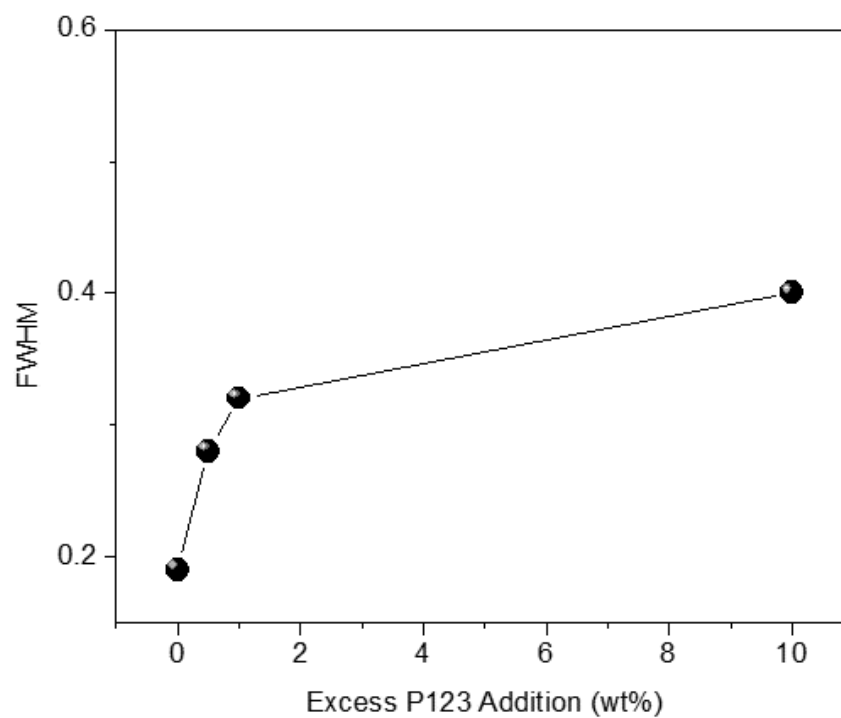


Figure S9. The change in the FWHM of the 110 XRD reflection with increasing amount of added P123.

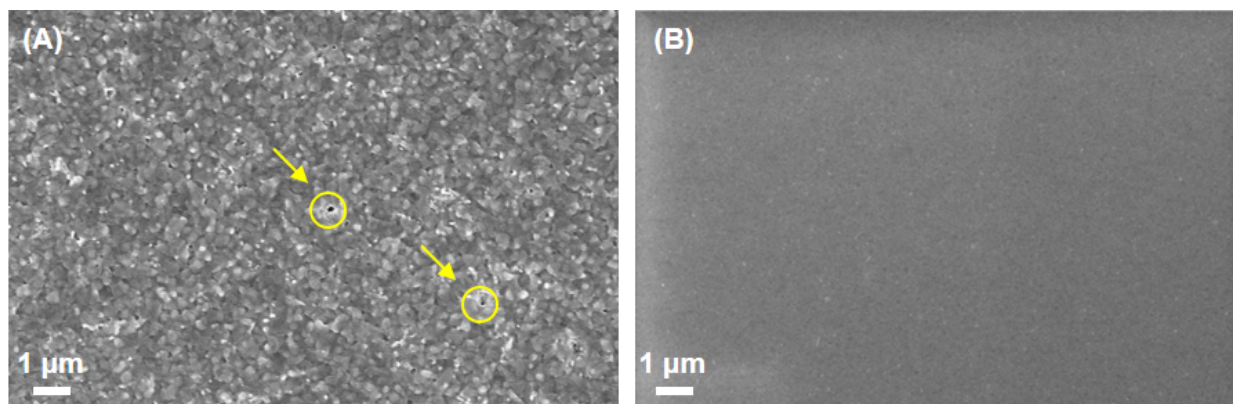


Figure S10. Lower-magnification top-view SEM images of: (A) MAPbI₃-0P and (B) -0.5P thin films. Occasional pinholes are observed in the MAPbI₃-0P thin film as indicated in (A), while the MAPbI₃-0.5P thin film is pinhole-free and ultrasmooth.

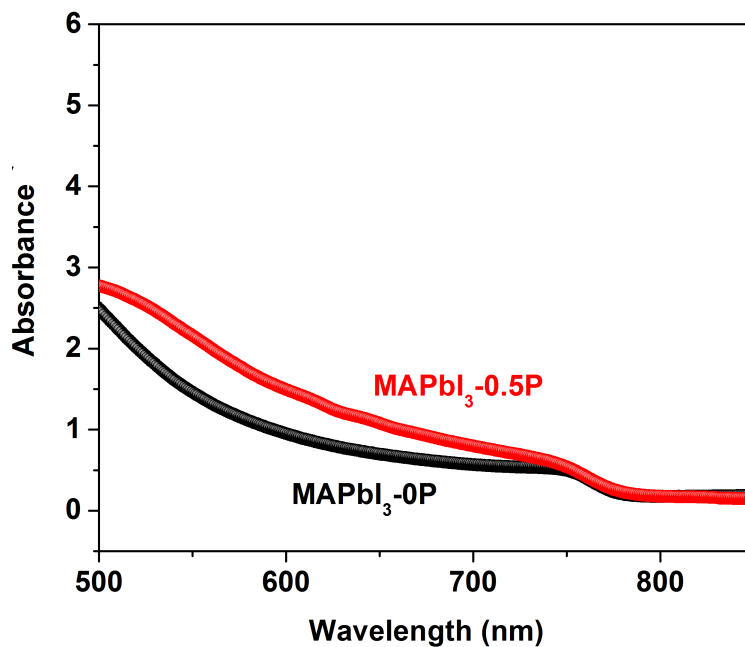


Figure S11. UV-*vis* absorption spectra of the MAPbI₃-0P and MAPbI₃-0.5P thin films.

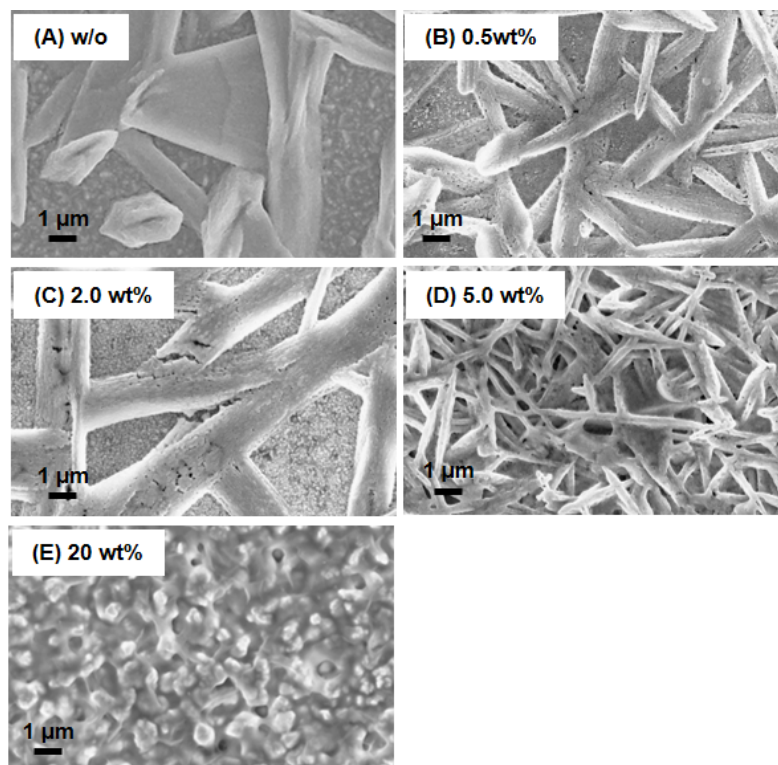


Figure S12. SEM images showing the surface morphologies of the MAPbI₃ thin films with increasing amount of added P123 that are prepared using the conventional one-step deposition method (without the (anti)solvent treatment).

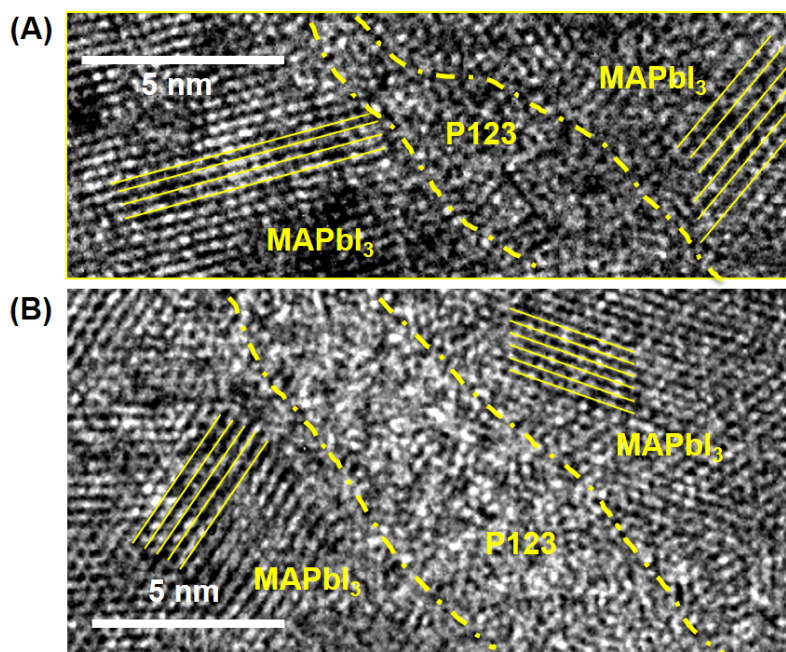


Figure S13. More detailed views of the GB regions based on a closer look at the TEM images of thin films: (A) MAPbI₃-0.5P and (B) MAPbI₃-1.0P thin films.

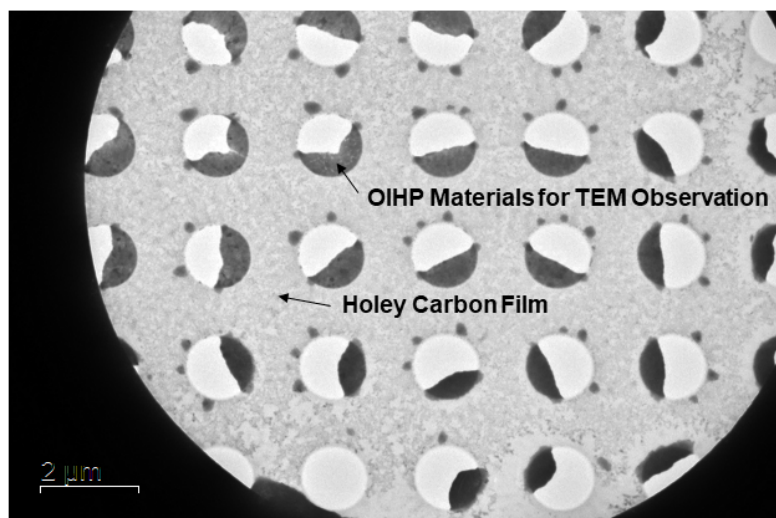


Figure S14. Low-magnification TEM image showing that the OIHP thin films are mainly on the carbon-coating-free area on the TEM grid making them free-standing.

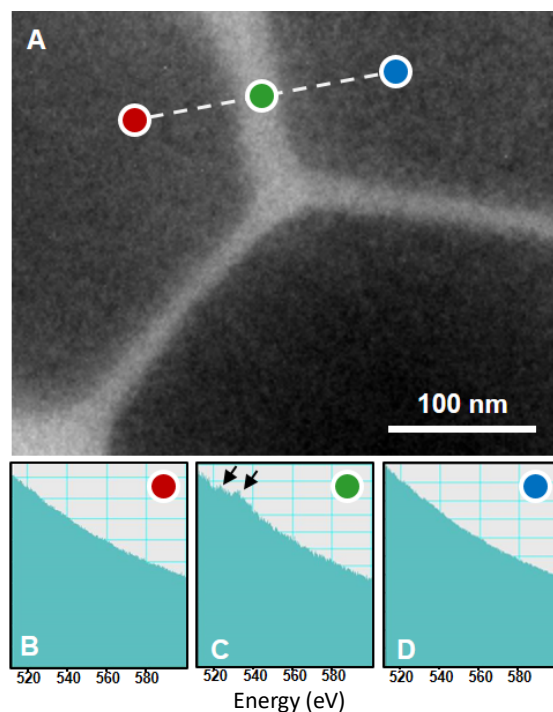


Figure S15. (A) TEM image of the MAPbI₃-10P sample. EELS spectra from the labelled regions: (B) and (D) from MAPbI₃ grains and (C) from amorphous GB region. Arrows in (C) mark O K-edge peaks. Note that this MAPbI₃-10P TEM sample shows relatively severe phase segregation mostly due to the large content of the P123 phase, resulting into locally-varied microstructures.

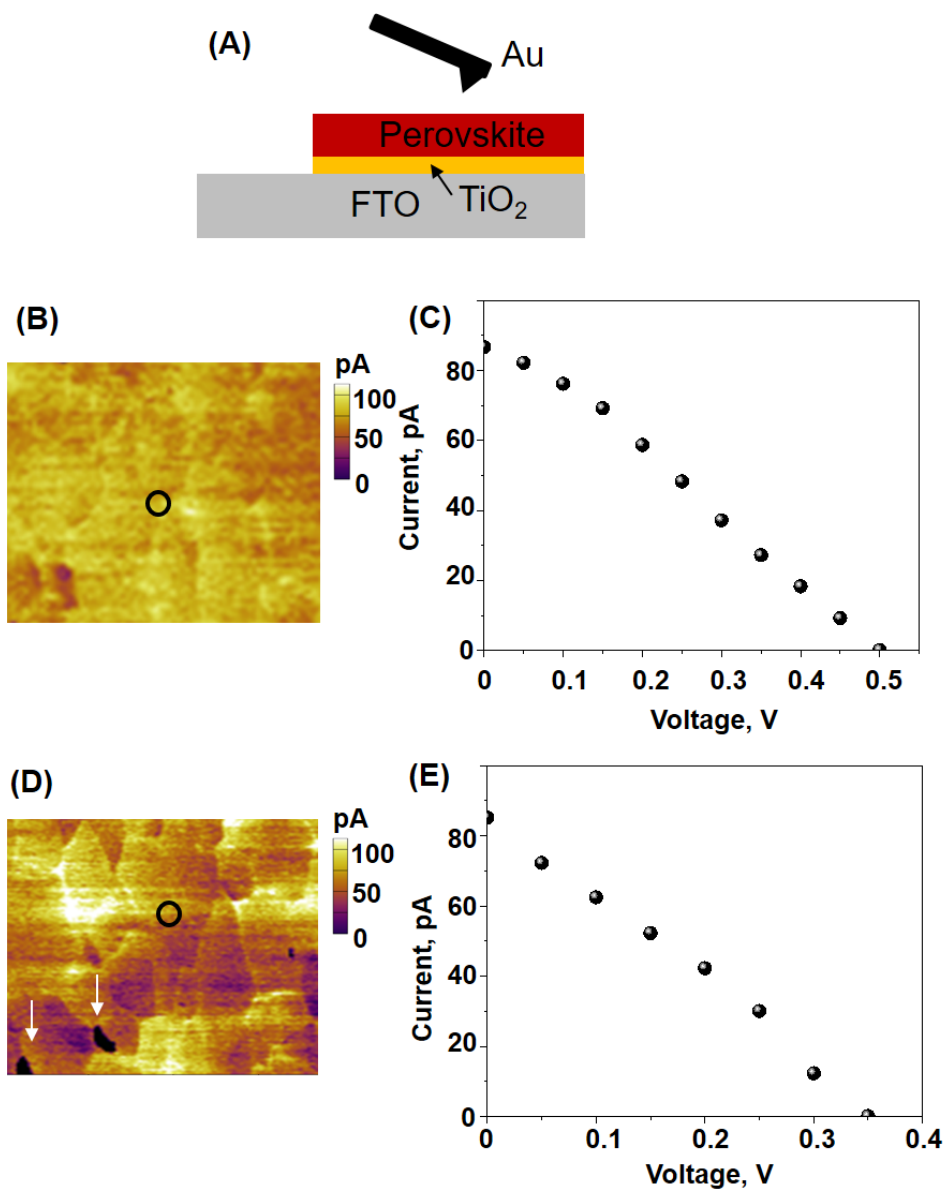


Figure S16. (A) Schematic illustration of the setup for the conducting AFM measurement. Photocurrent maps of thin films: (B) MAPbI₃-0.5P and (D) MAPbI₃-0P. Arrows in (D) indicate the photo-inactive areas where pinholes exist. Nanoscale *J-V* curves of: (C) MAPbI₃-0.5P thin film measured at location marked in (B) and (E) MAPbI₃-0P thin film measured at location marked in (D).

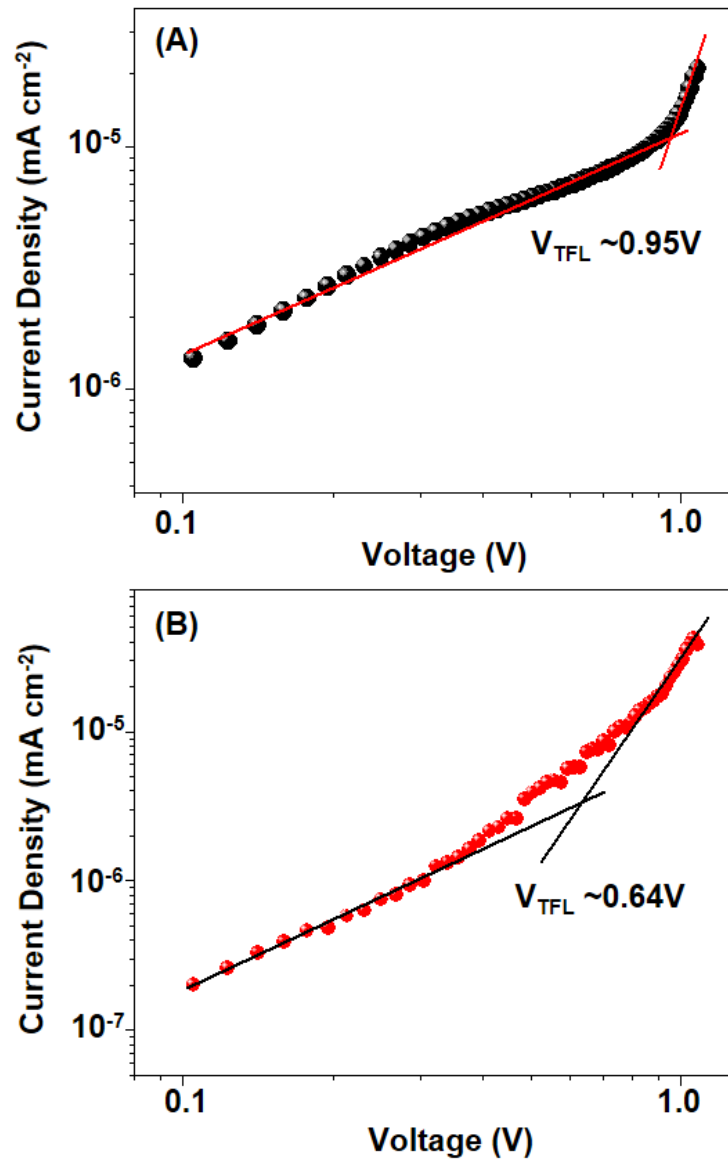


Figure S17. Dark current-voltage response of the MAPbI₃-0P and MAPbI₃-0.5P thin films in capacitor-like devices for estimating trap densities. The trap-filled limited voltages (V_{TFL}) are determined to be 0.95 V and 0.64 V, which correspond to trap densities of $4.97 \times 10^{16} \text{ cm}^{-3}$ and $3.35 \times 10^{16} \text{ cm}^{-3}$ for: (A) MAPbI₃-0P thin film and the (B) MAPbI₃-0.5P thin film, respectively.

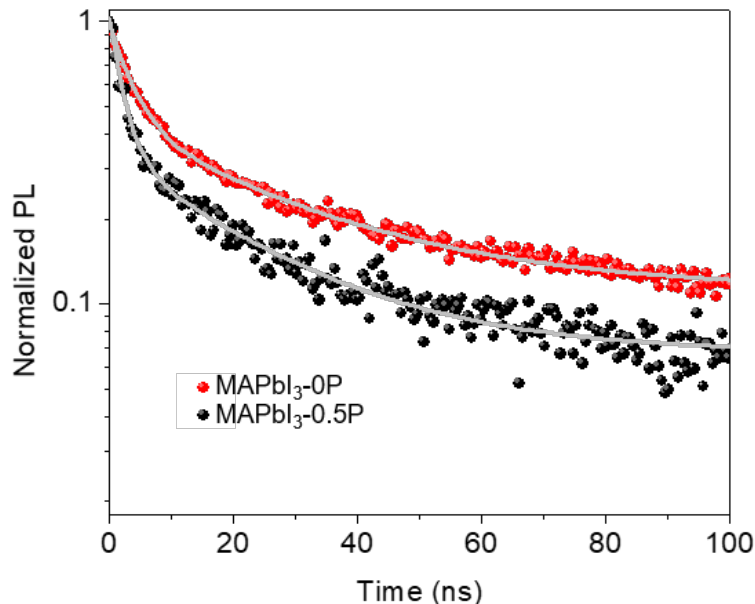


Figure S18. Time-resolved PL of the MAPbI₃-0P and MAPbI₃-0.5P thin films. The amplitude-weighted average lifetime for the MAPbI₃-0P and MAPbI₃-0.5P thin films is 9 and 12 ns, respectively.

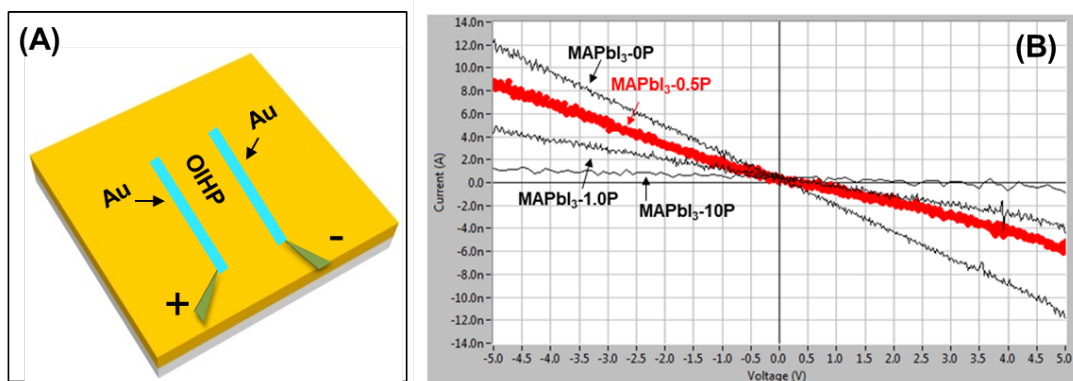


Figure S19. (A) Schematic illustration showing the device architecture for obtaining (B) I - V characteristics of MAPbI₃-0P, MAPbI₃-0.5P, MAPbI₃-1.0P, and MAPbI₃-10P thin films, which reflects the resistivity change with increasing amount of added P123. For fabrication of the devices, the OIHP thin films are deposited on the glass substrate according to the procedure described in the Methods section, followed by deposition of two identical Au electrodes (parallel) on top of the film top. For the I - V measurement, the voltage was scanned from -5.0 V to 5.0 V using a Keithley 2400 sourcemeter.

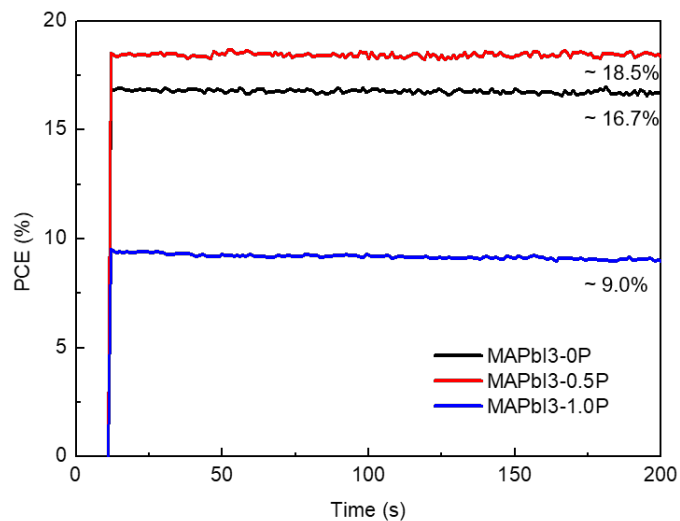


Figure S20. Stabilized maximum-power-point PCE outputs of PSCs based on the MAPbI₃-0P, MAPbI₃-0.5P, and MAPbI₃-1.0P thin films.

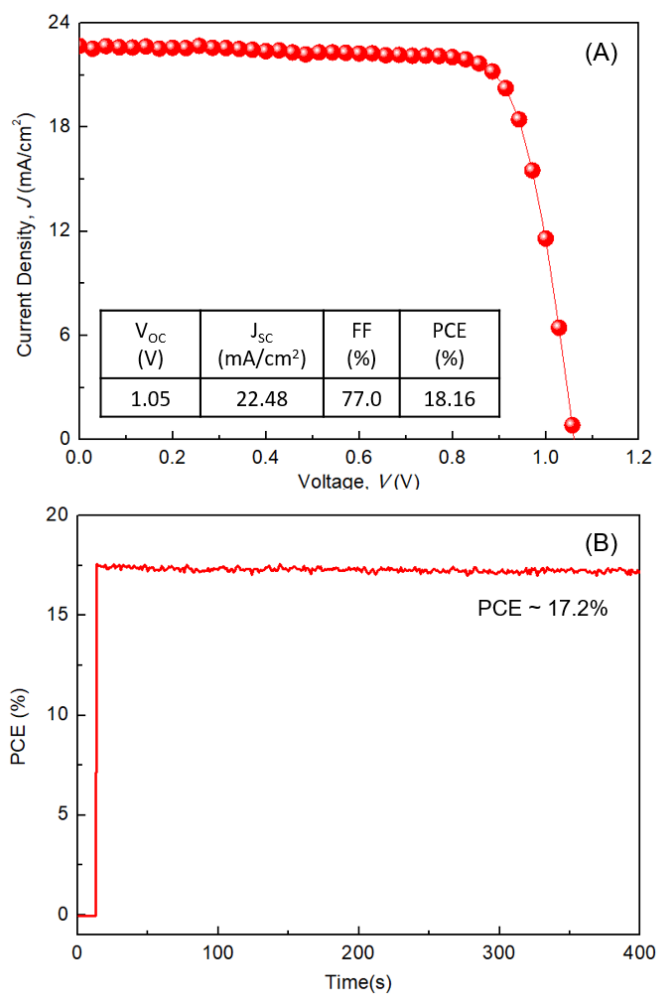


Figure S21. Typical PV performance of PSCs with incorporation of 0.1 wt % P123: (A) J - V response (reverse scan) and (B) stabilized maximum-power-point PCE output.

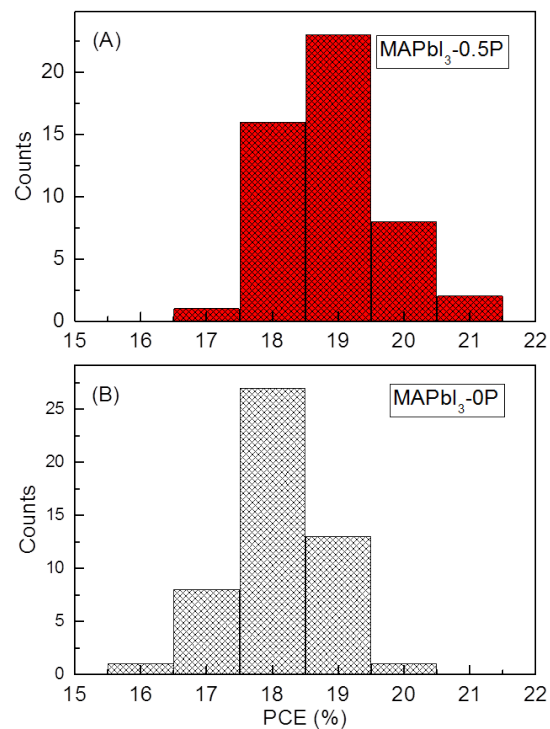


Figure S22. PCE statistics of PSCs based on the (A) MAPbI₃-0P and (B) MAPbI₃-0.5P thin films.

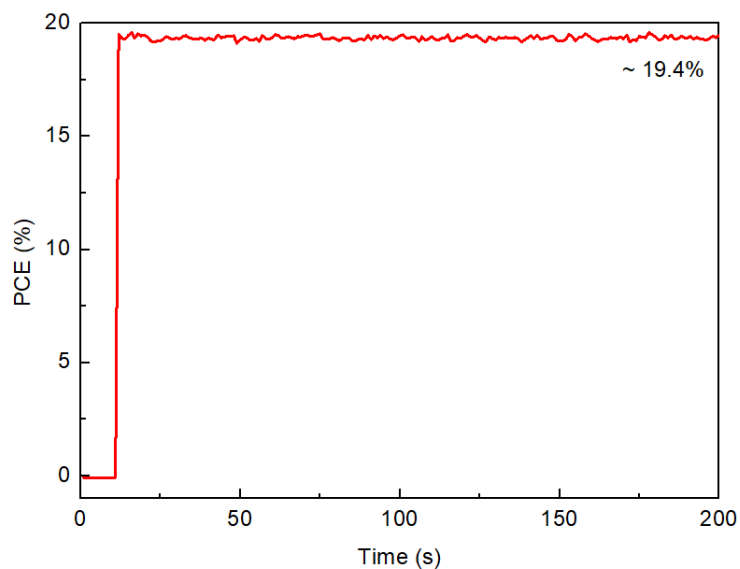


Figure S23. Stabilized maximum-power-point PCE outputs of the champion PSCs based on the MAPbI₃-0.5P thin film.

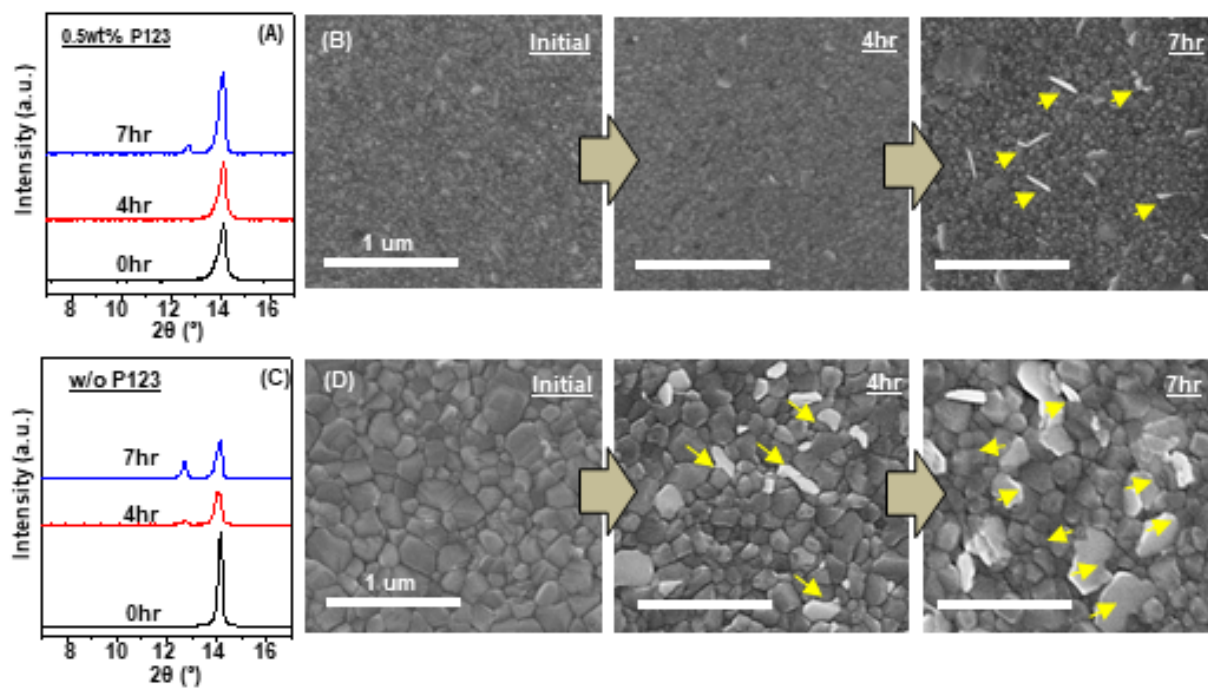


Figure S24. Sequence of XRD patterns and SEM images recording the progression of the degradation of thin films annealed at 100 $^\circ\text{C}$ in the ambient: (A, B) $\text{MAPbI}_3\text{-0.5P}$ and (C, D) $\text{MAPbI}_3\text{-0P}$.

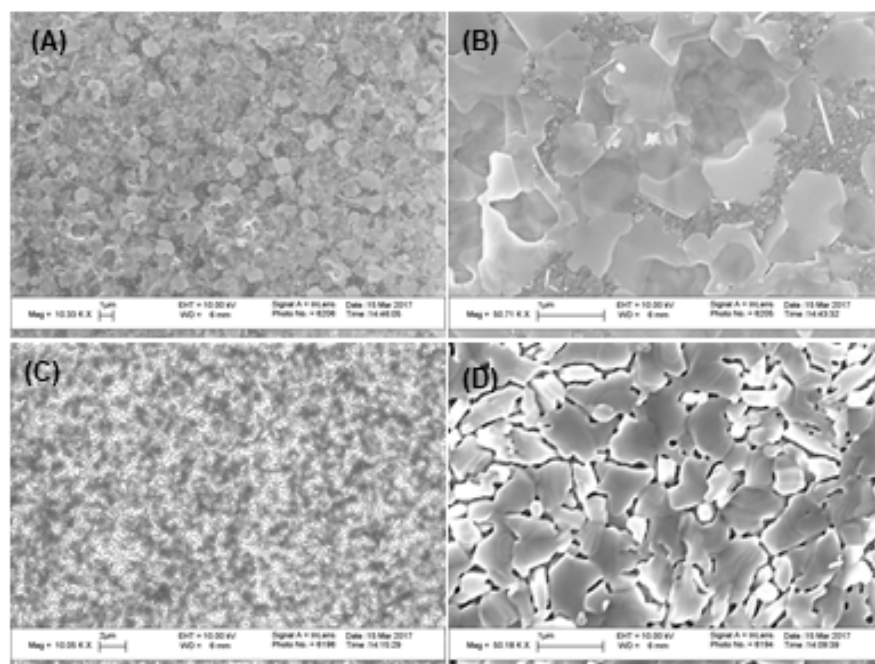


Figure S25. SEM images of the (A, B) $\text{MAPbI}_3\text{-0P}$ and (C, D) $\text{MAPbI}_3\text{-0.5P}$ thin films after 52-h annealing (100 $^\circ\text{C}$) in the ambient.

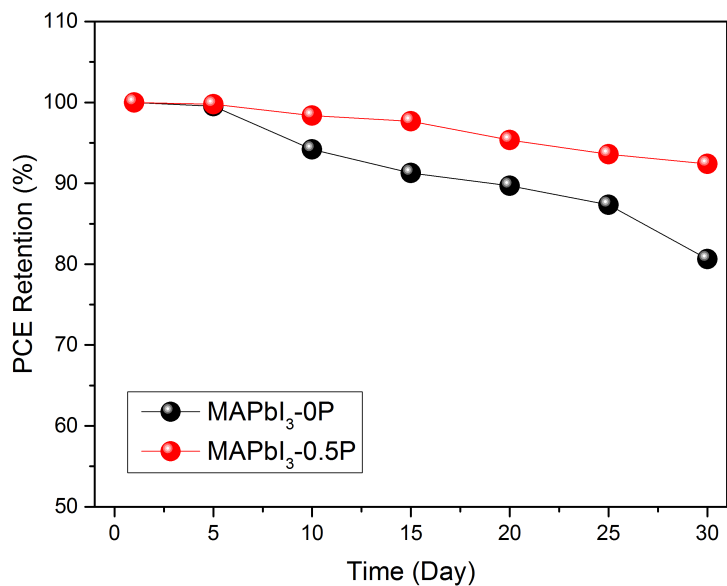


Figure S26. PCE evolution of PSCs based on the MAPbI₃-0P and MAPbI₃-0.5P thin films in the ambient (25% RH, RT)

Table S1. PV performance parameters that are extracted from the J - V curves (Figure 4B) of PSCs made using MAPbI₃-0P, MAPbI₃-0.5P, MAPbI₃-1.0P, and MAPbI₃-10P thin films.

PSC	V_{oc} (V)	J_{sc} (mA•cm ⁻²)	FF	PCE (%)
MAPbI ₃ -0P (R)	1.03	22.62	0.755	17.58
MAPbI ₃ -0.5P (R)	1.11	22.59	0.770	19.31
MAPbI ₃ -0.5P (R)	1.01	17.06	0.567	9.80
MAPbI ₃ -10P (R)	0	0	-	0